Operando Tracking of Transport Properties in Na 3 V 2 (PO 4) 2 F 3 and LiFePO 4 Battery Electrodes by In-Plane Measurements

Audrey Perju, Brinti Mondal, Victor Maurel, François Rabuel, Mathieu Morcrette, Pierre-Louis Taberna, Patrice Simon

Journal of The
Electrochemical Society

OPEN ACCESS

Operando Tracking of Transport Properties in $Na_3V_2(PO_4)_2F_3$ and $LiFePO_4$ Battery Electrodes by In-Plane Measurements

To cite this article: Audrey Perju *et al* 2024 *J. Electrochem. Soc.* **171** 110511

Journal of The Electrochemical Society, 2024 **171** 110511

Operando Tracking of Transport Properties in $Na_3V_2(PO_4)_2F_3$ and $LiFePO_4$ Battery Electrodes by In-Plane Measurements

Audrey Perju,[1,2] Brinti Mondal,[1,2] Victor Maurel,[1,2] François Rabuel,[2,3] Mathieu Morcrette,[2,3] Pierre-Louis Taberna,[1,2,z] and Patrice Simon[1,2,z]

[1] *Université de Toulouse III Paul Sabatier, CIRIMAT, UMR CNRS 5085, 118 Route de Narbonne, 31062, Toulouse cedex 9, France*
[2] *Réseau sur le Stockage Electrochimique de l'Energie (RS2E) FR CNRS, 3459, Amiens, France*
[3] *Université de Picardie Jules Verne, Laboratoire de réactivité et Chimie du Solide (LRCS), UMR CNRS 7314, 33 rue Saint Leu, 80000, Amiens, France*

The development of batteries has become a major challenge and requires new *operando* techniques for tracking reaction kinetics in battery electrodes during operation. Taking $Na_3V_2(PO_4)_2F_3$ and $LiFePO_4$ as examples of positive electrode materials, the present work deals with the design of an *operando* technique to measure the ionic and electronic transport properties of battery electrodes during polarization. In the case of $LiFePO_4$, large electronic resistance changes were revealed when crossing the solid-solution domains. Such resistance changes are consistent with thermodynamic models proposing the existence of a diffuse phase boundary between Li-poor and Li-rich domains, as a result of the non-linear variation of the chemical potential of the LFP particles, which in turn leads to restricted lithium diffusion. Concerning $Na_3V_2(PO_4)_2F_3$, the important variations of electronic resistance measured were correlated with different phase changes and superstructures formed during the insertion-disinsertion of Na^+ ions, as well as the polarization and entropy heat variations. These results are fully consistent with a substantial correlation of structural changes with transport properties and reaction kinetics, and thus, performances. More generally, this technique shows great promise as a tool to aid in designing battery electrodes with improved ionic and electronic percolations.
 [DOI: 10.1149/1945-7111/ad8d11]

Manuscript submitted September 13, 2024; revised manuscript received October 12, 2024. Published November 13, 2024.

Supplementary material for this article is available online

A key issue to further improve the performances of battery electrode materials is to develop the fundamental understanding of the charge storage/delivery mechanisms, driven by the electrochemical reaction kinetics. When phase separation is involved, composition heterogeneities arise, and the nucleation and growth of a new phase may depend on the rate, particle size and morphology, defects (…) and etc., resulting in modified ion diffusivity and/or electrical properties.[1–4] Moreover, interface domains formed during phase transitions usually come with volume changes and energy barriers, limiting the rate performances, whereas a smooth solid solution mechanism can lead to high-rate performances. A typical example is the widely studied $LiFePO_4$ cathode used in Li-ion batteries (LiBs), in which both phase separation and solid-solution can be identified depending on the rate or particle size.[5,6] Another example is the $Na_3V_2(PO_4)_2F_3$ cathode material for Na-ion batteries (NaBs), where a more complex charge/discharge mechanism has been identified, involving two-phase reactions, solid solution domains and various superstructures.[7]

The development of advanced characterization techniques has been of great importance to better understand the reaction mechanisms and paths in battery electrode materials, and LFP has been a candidate of choice for that aim. Several models have been proposed to describe the lithiation-delithiation process in FP/LFP particles, showing as a whole that solid solution (needing only low excess energy) is favoured at high scan rates and/or small particle size, and phase-separation happens at low scan rates and for largest particles.[8] Many experimental works have been conducted to study this phase-separation on single particle LFP, including using advanced high-resolution imaging/mapping techniques.[6,9–11] The existence of heterogenous reaction kinetics was revealed, resulting in asymmetric delithiation/lithiation behavior associated with the existence of an apparent phase separation as a dynamical artefact driven by autocatalytic electrochemical reactions.[9,11] The autocatalytic reaction path, and its autoinhibitory counterpart, were also evidenced in NMC lamellar oxide cathode materials, suggesting a general tendency for intercalation reactions.[12] These results demonstrate the importance of considering the strong concentration dependence of interfacial reaction kinetics.

However, while our understanding of reaction pathways and phase changes in battery materials is becoming increasingly sophisticated, we have little information about their influence on electrical properties during operation. This is all the more surprising given that optimizing electronic and ionic percolation within battery electrodes is necessary to boost their performances, especially for high-power delivery. There is then a need in developing new characterisation technics helping to understand better the changes of ionic and electronic percolation within the electrode while cycling, i.e., *operando*. Recently, we reported about a new experimental set-up designed for measuring *operando* the in-plane AC (Alternative Current) impedance and DC (Direct Current) resistance of capacitive electrodes during electrochemical charge-discharge experiments.[13] It is worth stressing the fact that, thanks to the in-plane configuration used, the measurements are highly sensitive to the changes of the electrode electrical properties, making this technique a powerful tool to characterize the ionic and electronic impedances within the electrodes during their polarization.

In the present study, we have developed further this experimental set-up to track *operando* the variations of the in-plane charge transport properties of carbon-coated $Na_3V_2(PO_4)_2F_3$ (NVPF) and $LiFePO_4$ (LFP) positive electrodes used in NaBs and LiBs, respectively. The possibility to track the changes of the electrode electrical properties upon cycling is of great importance to understand how to further improve the performances and how phase separations and phase transitions can be correlated to the transport properties. This set-up, in addition to being easy to implement, cost-effective, and space-efficient, has the potential to become a valuable tool for advancing our basic knowledge about the key factors controlling the change of the electrode resistance—and then kinetic—during battery operation.

Results and Discussion

In-plane impedance and resistance measurement set-up.— Electrodes were prepared by coating a mixture of carbon-coated

[z]E-mail: pierre-louis.taberna@univ-tlse3.fr; patrice.simon@univ-tlse3.fr

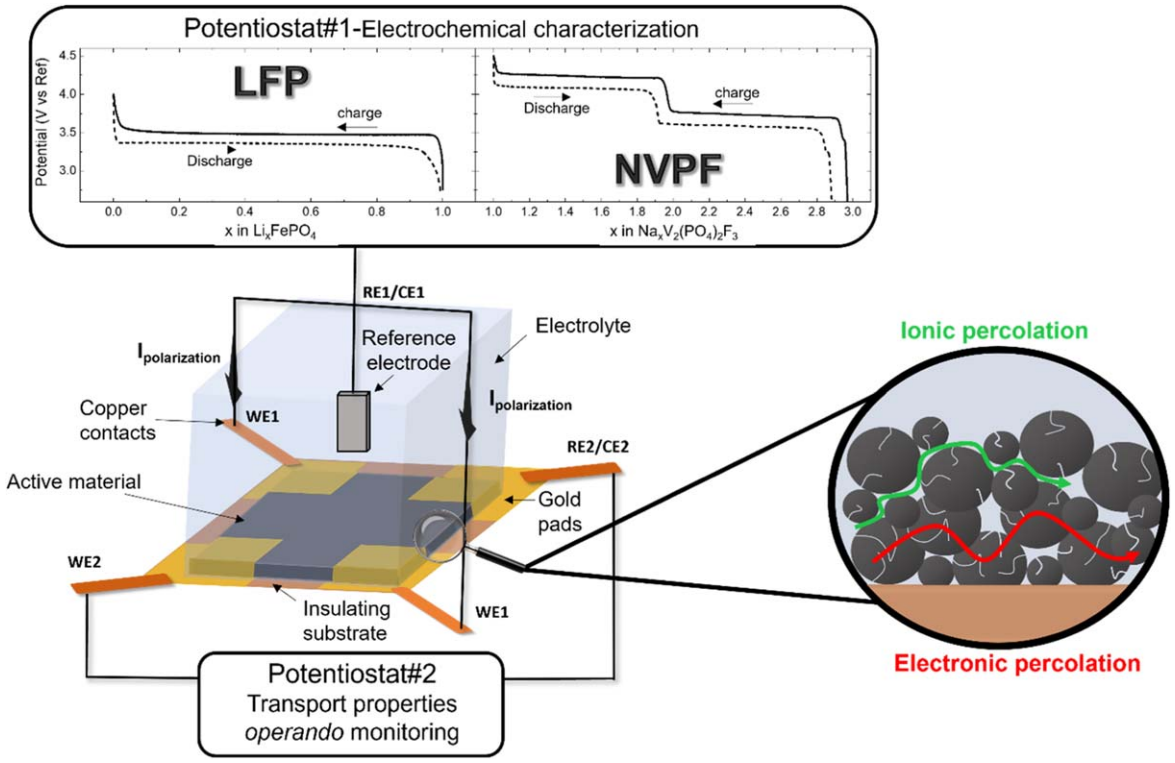

Figure 1. Setup used for in-plane *operando* tracking of the electrode electric transport properties with the utilization of two potentiostats: potentiostat#1 used to polarize the electrode and potentiostat#2 to perform the impedance/resistance measurements.

LFP or NVPF with carbon black as a conducting additive and PVDF binder onto an insulating polymer film (see Methods section). The complete setup is illustrated in Fig. 1 and in supplementary section S0, Fig. S0. Four gold pads were deposited (symmetrically) onto the four corners of the electrode, and used further to connect the potentiostats. Two different potentiostats were used in combination to perform the *operando* measurements: the first one was used to polarize the electrode (Fig. 1 potentiostat#1) and the second one to perform the in-plane impedance or resistance measurement (Fig. 1 potentiostat#2).

As shown in a recent paper dealing with capacitive electrodes,[13] such setup allows for tracking the electronic and ionic contributions using potentiostat#2, depending on the selected frequency range (electronic transport at low frequencies, and mostly ionic percolation at high frequencies). While under DC conditions (null frequency), only the changes of the electrode electronic percolation are measured. Importantly, to ensure reliable measurements, the electrode impedance must comply with an impedance accuracy contour plot (see Fig. S1), which defines the accuracy and reliability ranges of the in-plane measurements. This is particularly true at high frequencies, when it becomes possible to deal with both bulk electrolyte impedance and the ionic conductivity of the active material, that is the ionic conductivity in the electrode porosity. This plot shows that perturbations do not occur, as it is a crucial aspect of measurement reliability control. A measurement frequency of 300 Hz for the high-frequency *operando* impedance measurement for NVPF and LFP was then chosen to follow the evolution of the ionic transport upon cycling (Fig. S1). Indeed, as seen from the contour plots, the ionic percolation through the electrolyte bulk is more than five times than through the electrode at this frequency, and the later remains constant upon the entire high-frequency range, before being short-circuited by the electronic path at low frequency (Figs. S1 and S2). On the other hand, as observed in the contour plot (Fig. S1), the low-frequency region is perfectly out of any perturbations, and without any doubts, driven by the electronic percolation within the active material.

Regular in-plane EIS performed on NVPF and LFP electrodes, respectively in NP30 and LP30, are presented in Fig. S2. As reported in Fig. S3, the ionic impedances of the electrodes (measured at 300 Hz), mainly driven by the electrolyte resistance within the porous network between the particles, are kept unchanged with polarization and are at least one order of magnitude lower than the electronic impedance (measured at 100 mHz) for both materials (Fig. S2). Accordingly, the measurements were carried out in DC mode, as only the electronic transport is of interest and a better accuracy is expected. Indeed, significant variations in electronic transport were observed for both electrode materials.

As the measurements are carried out with the help of two potentiostats, it is important to ensure that there is no cross-talk between them. The validation of the experimental setup has been carefully made by running a series of experiments using three different configurations. A first one where potentiostat#1 was used to polarize the electrode while poentiostat#2 was disconnected (Fig. S4a, configuration A); a second one where potentiostat#1 was used for electrode polarization while potentiostat#2 was connected to measure in-plane OCV—meaning the potential difference between the two in-plane contacts—(Fig. S4a, configuration B) and finally, the last one where potentiostat#1 was used for electrode polarization while potentiostat#2 was applying a small constant current—few μA, as used to measure the in-plane electrode voltage drop to access the resistance—(Fig. S4a, configuration C). As reported in Figs. S4b and S4c, there were no perturbations in the recorded signals, and the galvanostatic curves were reproducible whatever the configuration used. Notably, as shown in Figs. S5a and S5b, significant changes in the in-plane voltage are measured while an in-plane current is applied with potentiostat#2 during the electrode polarization (Fig. S4a, configuration C); in contrast, no changes are observed for the in-plane OCV while the electrode is polarized (Fig. S4a, configuration B). This observation holds particular importance, as it demonstrates that the electrode plane is at the same potential when galvanostatic cycling is performed with potentiostat#1. Consequently, the voltage drop fluctuations obtained when applying

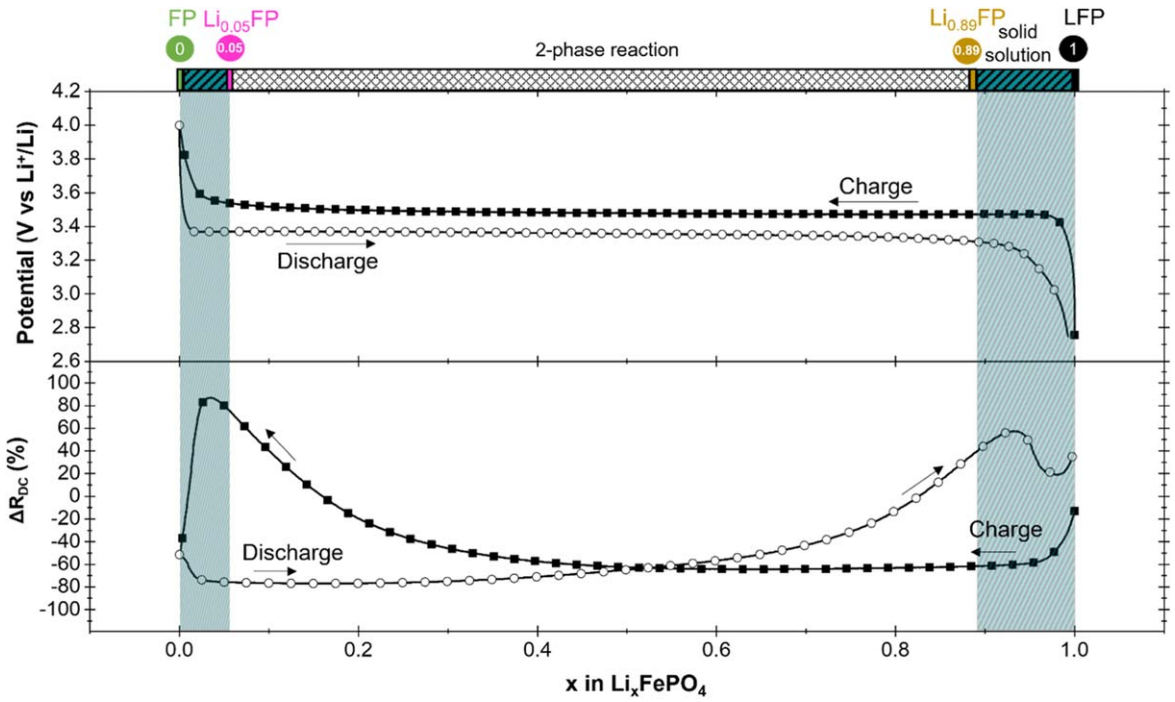

Figure 2. Galvanostatic cycling at a C/10 rate (using potentiostat#1, top panel) and in-plane DC resistance variations upon cycling of an LFP electrode in LP30 (potentiostat#2, bottom panel), correlated with XRD results obtained by Yamada et al.[14].

the in-plane current can be ascribed to active material's resistance variations. Finally, the ohmic behavior within the plane of the active layer was further confirmed between 0 and 100mV (Fig. S6). All these preliminary experiments confirm the reliability of the method.

In-plane resistance measurement of $LiFePO_4$ (LFP) electrodes during cycling.—Carbon-coated LFP (Fig. S7) is a well-known cathode material for LiBs used in a broad range of applications where safety, reliability, low cost and cyclability are required. *Operando* in-plane resistance measurements of the LFP composite electrode were achieved under DC condition, using the set-up presented in Fig. 1. Figure 2 (top panel) shows a charge-discharge galvanostatic cycling curve at a C/10 rate of the LFP electrode in LP30 electrolyte with Li metal as counter and reference electrode, achieved with potentiostat#1 (plotted vs the degree of lithiation, x, in Li_xFePO_4 with $0 < x < 1$). The galvanostatic cycling curve exhibits one main single plateau at about 3.45 V vs Li^+/Li, as shown in Fig. 2, top panel, corresponding to a two-phase Li^+ insertion/extraction into/from $FePO_4/LiFePO_4$ and the associated reduction/oxidation of iron.[14,15] Besides, in the hatched areas in Fig. 2 top panel corresponding to the end of charge/discharge, two regions with non-constant potential are observed, and have been assigned to the existence of a one-phase solid solution with Li ions insertion/extraction into/from $Li_xFePO_4/Li_{1-x}FePO_4$.[14] Overall, the charge storage mechanism has been reported as follows (Eqs. 1–3):

Solid solution, for $0 < x < 0.05$:

$$FePO_4 + xLi^+ + xe^- \rightleftarrows Li_xFePO_4 \quad [1]$$

2-phase plateau for $0.05 < x < 0.89$:

$$FePO_4 + xLi^+ + xe^- \rightleftarrows xLiFePO_4 + (1-x)FePO_4 \quad [2]$$

Solid solution, for $0.89 < x < 1$:

$$Li_xFePO_4 + (1-x)Li^+ + (1-x)e^- \rightleftarrows LiFePO_4 \quad [3]$$

During cycling with potentiostat#1, a constant current, I_{cp}, is applied in the plane of the electrode using potentiostat#2. The in-plane electrode resistance was obtained by dividing the resulting in-plane voltage drop, ΔV_{cp}, by the constant polarization current, I_{cp} (see Supplementary section 2 and Methods section). Figure 2 bottom panel shows the relative resistance variations calculated using Eq. S3, with the degree of lithiation x (x in Li_xFePO_4 with $0 < x < 1$). The resistance values obtained during this *operando* DC resistance measurement (in kΩ) are shown in Fig. S8a.

Fundamentally, the electronic resistance of the electrode film made with powder material has two main contributions: the intrinsic bulk particle resistance and the resistance at the grain-grain contact interface. Consequently, any variations in the carbon-coated LFP composite resistance, which can result from factors like doping or structural evolutions during polarization, will result in a change of the electrode in-plane resistance. Additionally, electrode resistance fluctuations may also be linked to changes in the grain-grain contact impedance, stemming from shifts in resistivity or volume changes of the LFP active film.

The electrode in-plane resistance measurement shows peculiar variations; on average, the L_xFP electronic resistance is higher for $x = 1$ than for $x = 0$, in agreement with the electronic resistance of $LiFePO_4$ and $FePO_4$[16] and theoretical calculations.[17] In-plane resistance measurements on the electrodes with various LFP/conductive carbon content were achieved (Fig. S9) to unambiguously assign the resistance changes of the 80% LFP-10% carbon-10% PVDF composite in Fig. 2 to the conductivity or percolation changes of the carbon-coated LFP particles.

The local variations of the LFP electrode resistance with x in Fig. 2 bottom panel is not linear and, importantly, shows an asymmetric pattern with clear path dependency in the solid-solution zones. Indeed, for the charging process (from 1 to 0 lithium, black line with square marker), a first drop in resistance occurs at a very low delithiation state ($x = 1$ to $x = 0.95$), corresponding to the galvanostatic area where the potential is reaching the plateau region. Following this, the resistance remains fairly constant until $x = 0.4$ where it starts to sharply increase until reaching a maximum at $x = 0.03$, highly delithiated state. Then, the resistance drops steeply when the LFP gets fully delithiated. Concerning the discharge process (from 0 to 1 lithium, black line with hollow circle marker),

the resistance decreases slightly from the $FePO_4$ phase to a lithium content around 0.02, before increasing drastically up to $x = 0.93$ where a resistance peak is observed.

Overall, it seems that two regimes can be identified on Fig. 2 bottom panel: one linked to the solid solution region (hatched areas for composition ranges corresponding to very high or very low lithiation rates, ($x < 0.05$ and $x > 0.89$,[14] see Eqs. 1 and 3 above), where the resistance has a strong non-linear behaviour, and another one in the plateau region—associated with a biphasic reaction ($0.05 < x < 0.89$,[14] see Eq. 2 above)—where the resistance variation is quite linear.

To describe the charge/discharge processes occurring within LFP particles while cycling, several mechanisms have been proposed over the years. The first one is based on a core–shell model, where the Li-rich and Li-poor phases are respectively located in the surface/heart of the particle and the delithiation/lithiation occurs through the shell with a displacement of the phase boundary.[18,19] This model was further improved, and the "domino cascade" model was proposed, suggesting a fast movement of the boundary leading to the existence of mostly either fully lithiated or delithiated particles.[20,21] However, it failed short to explain the high-rate dependency on the cycling-history reported in several studies,[22,23] which depends on many parameters like the miscibility gap of both phases—mostly determined by the particle size and temperature–, the synthesis method and surface coating, and the experimental cycling conditions.[24] Additionally, none of these models can explain the presence of the strong nonlinear and path dependency profile of the electrode resistance that we recorded during both lithiation and delithiation.

The concept of Coupled Ion-Electron Transfer (CIET), recently proposed by Bazant et al. for LFP material,[9,25] that considers the simultaneous transfer of ions and electrons and the associated energy landscape, can also nicely explain the resistance variations in LFP composite electrode, as the result of the potential gradient and heterogeneity of composition between LFP particles. This potential gradient depends on the lithiation/delithiation path that the particles will take, being itself dependent on the reaction kinetic (i.e. the current, driving the reaction rate), as well as the quality of the carbon coating.[9] In the plateau region, where resistance variations are recorded despite the supposed biphasic mechanism, a composition gradient may start to form as the resistance increases upon lithium insertion/deinsertion, reaching a maximum at the end of the plateau. When the solid-solution region with non-constant potential is reached, an autocatalytic/autoinhibitory process can explain the observed resistance change. The change of the exchange current density in the CEIT theory defines two domains for Li intercalation and deintercalation in LFP electrodes, with a maximum value at about $x \approx 0.4$ Li. As a result, both Li insertion at high lithiated states and Li deinsertion from Li-poor phase are achieved under the autoinhibitory regime, while the reverse reactions - Li insertion in the Li-poor phase and Li removal from the Li-rich phase—are autocatalytic.

Starting from fully discharged LFP ($x = 1$), the initial resistance drop during charge follows the autocatalytic process, as Li removal from a full structure is easier thanks to repulsive interactions between highly concentrated intercalated Li ions. This autocatalytic process causes instability in concentration and increases internal domain wall mobility in the particle structure, resulting in a resistance decrease. Then, when reaching low lithiation states at the end of the charge, the CEIT process becomes mainly auto-inhibitory as Li removal from Li-poor structure is less energetically favorable due to increasing repulsive interactions between Li vacancy sites. The autoinhibitory process, achieved at low exchange current density, results in the freezing of the internal domain structure as also demonstrated by Wagemaker et al.,[10] leading to the large resistance increase reported in Fig. 2. The decrease in resistance observed during the charge at a low lithiation state ($x < 0.02$) in Fig. 2 could be explained by the higher electronic conductivity of the carbon-coated FP vs LFP, which drives the electrode electrical property. Similarly, when switching the current to discharge, the potential reaches 3.45 V and the resistance decreases in agreement with the autocatalytic process; it finally increases at the end of the discharge, when the autoinhibitory process controls the kinetics.

To summarize, the in-plane resistance results show that the electronic charge transport in LFP is correlated with the electrode reaction kinetics during operation. More specifically, the resistance changes of the LFP composite electrode shows an asymmetric behavior with important resistance change in the solid solution domains, that is at high and low lithiated states. This path dependency of the resistance well agrees with the concept of CIET recently proposed in the literature and generalized to several electrode materials, which suggests the existence of autocatalytic electrochemical reactions occurring in a many-particle system, resulting in an interfacial exchange current that increases with the extent of delithiation. Inversely, the lithiation of a lithium-rich phase at the end of the charge is driven by an autoinhibitory electrochemical reaction that increases the resistance.

In-plane resistance measurement of $Na_3V_2(PO_4)_2F_3$ (NVPF) electrodes during cycling.—NVPF is a polyanionic material, demonstrating a strong competitiveness in the pursuit of post LiBs advancements. Addressing the issue of material availability while maintaining a low cost, NVPF is now used as a positive electrode in commercial Na-ion batteries,[26] which are now under extensive development thanks to their key features such as high-power capability, including fast charge.

Operando in-plane resistance measurement of the NVPF electrode was achieved in the same way as for the LFP electrode, under DC condition using the set-up presented in Fig. 1. Figure 3 (top panel) shows the charge-discharge galvanostatic cycling curve at a C/10 rate of the NVPF electrode in NP30 electrolyte with Na metal as counter and reference electrode, achieved with potentiostat#1 (plotted vs the degree of sodiation, x, in $Na_xV_2(PO_4)_2F_3$ with $1 < x < 3$). The bottom panel of Fig. 3 shows the relative resistance variations with the degree of sodiation, x, (normalized to 3 sodium, see supplementary section S2) in $Na_xV_2(PO_4)_2F_3$, calculated using Eq. S3. The resistance values obtained during this *operando* DC resistance measurement (in kΩ) are shown in Fig. S8b.

The galvanostatic charge-discharge plot recorded with potentiostat#1 shows the expected electrochemical signature with two plateaus around 3.7 and 4.2 V vs Na^+/Na, corresponding to the insertion/extraction of 2 Na^+ in/from NVPF and the associated reduction/oxidation of Vanadium (Eqs. 4 and 5):

$$Na_3V_2(PO_4)_2F_3 \rightleftarrows Na_2V_2(PO_4)_2F_3 + Na^+ + e^- \quad \text{(plateau around 3.7 V vs } Na^+/Na) \qquad [4]$$

$$Na_2V_2(PO_4)_2F_3 \rightleftarrows NaV_2(PO_4)_2F_3 + Na^+ + e^- \quad \text{(plateau around 4.2 V vs } Na^+/Na) \qquad [5]$$

Bianchini et al. have reported structural changes of NVPF occurring during constant current charge-discharge by performing a high-resolution synchrotron X-ray diffraction study.[7] In charge, from the composition $Na_3V_2(PO_4)_2F_3$ to $Na_{2.4}V_2(PO_4)_2F_3$ ($3 > x > 2.4$), they firstly observed that the Na deintercalation reaction progresses through various intermediate (metastable) states, with a partial ordering of the sodium on the short-term range. Moreover, they identified the formation of a not fully stabilized superstructure at the composition $Na_{2.4}V_2(PO_4)_2F_3$, still containing unordered domains, with a doubling of the unit cell parameters. Upon further charge, they identified the $Na_2V_2(PO_4)_2F_3$ composition as a superstructure involving a huge cell parameter increase, related to sodium ions and vanadium cations ordering.[7] Finally, during the removal of the last Na from $Na_2V_2(PO_4)_2F_3$ to $Na_1V_2(PO_4)_2F_3$, they were able to identify a monophasic solid solution domain in the $1.3 < x < 1.8$ composition range.[7]

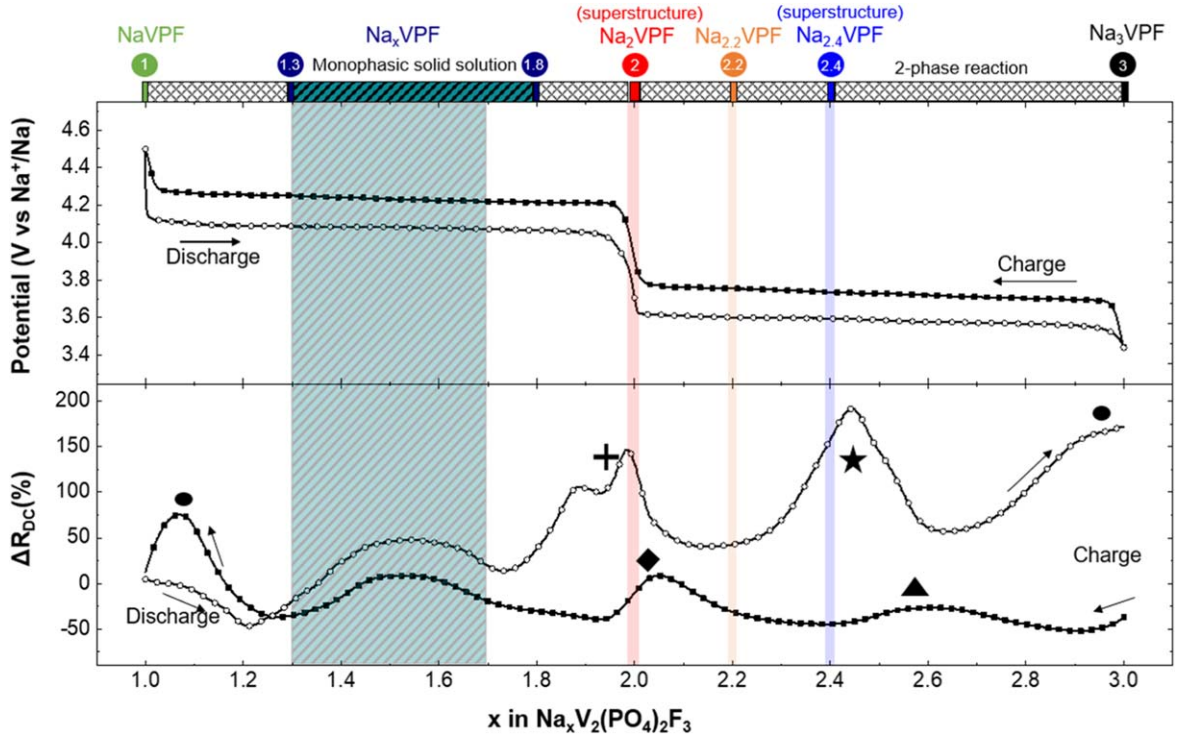

Figure 3. Galvanostatic cycling at a C/10 rate (potentiostat#1, top panel) and in-plane DC resistance variations upon cycling (potentiostat#2, bottom panel) of an NVPF electrode in NP30, consistent with synchrotron results obtained by Bianchini et al.[7]

Those observations nicely correlate with the resistance variations observed in the present work. Going more into details, after a first decrease in resistance at the beginning of the charge (black line with square markers), a resistance peak can be observed in Fig. 3 bottom panel, at about x = 2.58 sodium (black triangle marker), followed by another resistance peak around x = 2.0 (black diamond-shaped marker), corresponding to the removal of the first Na ion from the NVPF structure. These features can be associated with the reported $Na_{2.4}V_2(PO_4)_2F_3$ and $Na_2V_2(PO_4)_2F_3$ superstructures, with consequent cell volume increase. While continuing charge, a broad resistance peak shows up within the $1.7 > x > 1.4$ composition range (hatched area), corresponding to the monophasic solid-solution domain identified by Bianchini et al.[7] Then, a last resistance peak is observed at the end of the charge (left black dot marker), when the second Na is removed, corresponding to the $NaV_2(PO_4)_2F_3$ composition, which at first sight cannot be directly associated with any phase change.

During discharge (black line with hollow circle marker), in a symmetric way, Na ion intercalation starts with a small decrease in resistance from x = 1 to x = 1.2. Then, a broad resistance peak appears between 1.3 and 1.7 Na, mirroring the charge process. The resistance peak appearing at the transition between the two potential plateaus is still present, although slightly shifted, now around 1.85 sodium (black cross marker). A second peak is now clearly visible during this transition, while both peaks were merged during charge, resulting in an asymmetric shape. Upon further discharge, a sharp resistance peak around x = 2.35, corresponding to the $Na_{2.35}V_2(PO_4)_2F_3$ composition, is visible (black star marker). This peak is then followed by a last increase in resistance while reaching the end of the second discharge plateau (right black dot marker). A slight shift in the composition is observed for some resistance peaks compared to the compositions reported by Bianchini et al.,[7] but this could be explained by the difference in data acquisition mode, as our measurements are done under transient conditions (*operando,* while the electrode is charging and discharging), while the in situ XRD experiments were made under steady state (GITT measurements including a relaxation step between two constant current measurements).

Remarkably, our resistance measurement also nicely echoes calorimetric data recently reported,[27] inferring from optical fiber sensors. By incorporating optical fiber Bragg grating sensors inside 18650 Na-ion cells using NVPF as positive electrodes, Huang et al. were able to measure the total heat exchange during galvanostatic charge-discharge cycling of the cell. The total heat was further decomposed into overpotential heat (the irreversible heat due to the overpotential of the main reaction) and entropy heat contributions. Interestingly, the overpotential heat contribution attributed to the ion transport component shows the presence of two peaks at the beginning of charge and end of discharge,[27] and we also observed an increase of the resistance at both the end of charge (around x = 1.1, left black dot marker in Fig. 3 bottom panel) and end of discharge (x = 2.8, right black dot marker in Fig. 3 bottom panel), which could not be directly associated with any phase changes. This suggests that these resistance peaks might come from the large amount of heat released at the end of charge and at the end of discharge, stemming primarily from Na ion diffusion limitations (e.g., sluggish diffusion of Na ions) in the NVPF structure. From a global view, the Na ion diffusion limitations responsible for the overpotential heat contribution at the beginning of charge and end of discharge[27] is also consistent with the previously described "auto-inhibitory" process of the CIET, where the strong repulsion interaction between the inserted Na cations in the structure at the end of discharge or the increase repulsive interactions between Na vacancy sites at the end of charge decreases the exchange current density j_0.[9,11,25]

To summarize, the changes in the in-plane electronic percolation of the electrode align well with the structural phase transitions of NVPF. This is coupled with contributions from overpotential and entropy heat at high and low sodium content, the latter likely arising from the autocatalytic or autoinhibitory reaction concept, resulting in resistance path dependency at both extreme composition ranges.[9,11,27] While a contribution of the volume variations occurring within the NVPF electrode resulting from phase transformations during cycling cannot be completely ruled out, the results clearly show that the changes in the in-plane electronic conductivity of the

electrode is correlated with phase transformations, as well as the Na ion diffusion in the solid phases. Additionally, whereas the electronic transport undergoes substantial variations that our in-plane resistance measurement technique was able to clearly evidence, conversely, the ionic percolation between the particles remains relatively constant throughout the cycling process for both materials (Fig. S3). Lastly, the technique offers the possibility to run *operando* AC impedance measurements at low frequency (100 mHz), as shown in Fig. S10, to access the phase angle changes (capacitive contributions associated with the grain-grain contact impedance) during polarization. While it does not bring additional information in the case of LFP and NVPF, measuring the imaginary part of the impedance could be interesting for other materials where the interface contributions are emphasized, such as in electrode composite for solid-state batteries.

Conclusions

Two battery cathode materials have been investigated with the help of a new set-up allowing *operando* tracking of the electrical properties of the layer. In both materials, electronic resistance has been identified as the dominant factor influencing the overall transport properties. In the case of LFP, we observed an asymmetric change of the resistance associated with important resistance variations in the solid solution domains. This path dependency of the resistance is consistent with the Coupled Ion-Electron Transfer (CIET) theory, where autocatalytic or inhibitory reactions occur in the extreme composition domains (highly lithiated or delithiated states). For NVPF, in-plane electrode resistance variations were first observed at compositions matching with solid solution domains and formation of superstructures, showing that the electronic transport properties of the active material are therefore not the same depending on the sodium content in the NVPF structure. Important resistance changes were also recorded at both the end of charge and discharge, in agreement with calorimetry measurements, suggesting that the redox processes at both extreme composition ranges are likely controlled by the CIET. Finally, the results presented above highlight the significant value of the operando in-plane impedance/resistance measurement technique in characterizing the electrical properties of battery electrodes during operation. This approach provides insights into how phase changes are correlated with electronic percolation and reaction kinetics, offering promising perspectives for optimizing electrode formulations and enhancing power performance.

Methods

NVPF electrodes preparation.—Optimized electrodes made of 91% carbon-coated $Na_3V_2(PO_4)_2F_3$, 6% carbon conducting additive and 3% PVDF binder were coated by Doctor Blade onto polyethylene film. The thickness of the calendared electrode was around $e = 110\,\mu m$. 4 mm square electrodes were then cut and gold pads were sputtered on the four corners of the sample to enhance the contact between the active material and the cell's connections.

LFP electrodes preparation.—LFP carbon-coated powder was mixed with carbon conducting additive and PVDF in a ratio of 80/10/10 (active material/carbon black/binder), and then coated by Doctor Blade onto Kapton® film. The electrode thickness was around $e = 20\,\mu m$. Similarly to NVPF electrodes, 4 mm square electrodes were then cut and gold pads were sputtered on the four corners of the sample.

Electrochemical characterization.—All NVPF and LFP samples were electrochemically characterized in 1 M $NaPF_6$ in EC:DMC 1:1 vol (NP30) with 2%wt Fluoroethylene carbonate and 1 M $LiPF_6$ in EC:DMC 1:1 vol (LP30) respectively, using a 2-electrode set-up, where the electrode film was the working electrode. A metallic sodium wire for NVPF and lithium wire for LFP was used as counter and reference electrode. Galvanostatic charge-discharge curves and cyclic voltammetry were obtained by using potentiostat#1 of Fig. 1 and the current was adjusted to achieve a 10 h charging time. All galvanostatic cycling was performed using either a SP200 or a VSP300 potentiostat/galvanostat from BioLogic. Cyclic voltammetry has been performed using a Metrohm Autolab Vionic potentiostat/galvanostat.

In-plane EIS and operando DC resistance measurement.—All in-plane Electrochemical Impedance Spectroscopy (EIS) and in-plane resistance measurements were performed with a potentiostat/galvanostat/ZRA interface 1010B from GAMRY instruments (potentiostats#2 in Fig. 1). The changes in the in-plane resistance of the electrode upon cycling were measured using the complete electrochemical setup depicted in Fig. 1, utilizing the two potentiostats. Potentiostat#2 was then used to perform a chronopotentiometry by applying a small current ($I_{cp} = 1\,\mu A$) while recording the voltage drop ΔV_{cp} (during the cycling of the sample through potentiostat#1) to allow accessing the DC resistance through Ohm's law. The voltage recorded with potentiostat#2 was then corrected from the potential variations coming for polarization heterogeneities within the electrode by subtracting the in-plane potential variations (in-plane OCV) measured during cycling in the absence of any DC current (see Supplementary section S2). Finally, all resistances were converted into relative percentage variations to normalize the results. More details about the data treatment are provided in the Supplementary section S2.

Acknowledgments

A. P. and B.M. were supported by a CNRS PhD grant. P. L. T., and P. S. thank the support of the Agence Nationale de la Recherche (Labex Store-ex) and the ERC Synergy Grant MoMa-Stor #951513.

Credit Authorship Contribution Statement

P-L. T. and P. S. designed the research plan. A.P., and B.M. conducted the experiments. All authors contributed to the discussion and prepared the manuscript.

Declaration of Competing Interest

The authors declare no competing interests.

ORCID

Patrice Simon https://orcid.org/0000-0002-0461-8268

References

1. C. Wang and J. Hong, *Electrochem. Solid-State Lett.*, **10**, A65 (2007).
2. J. Molenda, *Solid State Ion.*, **36**, 53 (1989).
3. J. Ma, C. Wang, and S. Wroblewski, *J. Power Sources*, **164**, 849 (2007).
4. K. Chayambuka, G. Mulder, D. L. Danilov, and P. H. L. Notten, *J. Power Sources Adv.*, **9**, 100056 (2021).
5. M. Wagemaker et al., *J. Am. Chem. Soc.*, **133**, 10222 (2011).
6. N. Ohmer et al., *Nat. Commun.*, **6**, 6045 (2015).
7. M. Bianchini et al., *Chem. Mater.*, **27**, 3009 (2015).
8. H. Liu et al., *Science*, **344**, 1252817 (2014).
9. H. Zhao et al., *Nature*, **621**, 289 (2023).
10. X. Zhang et al., *Nat. Commun.*, **6**, 8333 (2015).
11. M. Z. Bazant, *Faraday Discuss.*, **199**, 423 (2017).
12. J. Park et al., *Nat. Mater.*, **20**, 991 (2021).
13. V. Maurel et al., *J. Electrochem. Soc.*, **169**, 120510 (2022).
14. A. Yamada et al., *Nat. Mater.*, **5**, 357 (2006).
15. M. Hess, T. Sasaki, C. Villevieille, and P. Novák, *Nat. Commun.*, **6**, 8169 (2015).
16. C. Zhu, K. Weichert, and J. Maier, *Adv. Funct. Mater.*, **21**, 1917 (2011).
17. T. Maxisch, F. Zhou, and G. Ceder, *Phys. Rev. B*, **73**, 104301 (2006).
18. A. K. Padhi, K. S. Nanjundaswamy, and J. B. Goodenough, *J. Electrochem. Soc.*, **144**, 1188 (1997).
19. V. Srinivasan and J. Newman, *J. Electrochem. Soc.*, **151**, A1517 (2004).
20. C. Delmas, M. Maccario, L. Croguennec, F. L. Cras, and F. Weill, *Nat. Mater.*, **7**, 665 (2008).
21. G. Brunetti et al., *Chem. Mater.*, **23**, 4515 (2011).
22. V. Srinivasan and J. Newman, *Electrochem. Solid-State Lett.*, **9**, A110 (2006).
23. T. Sasaki, Y. Ukyo, and P. Novák, *Nat. Mater.*, **12**, 569 (2013).
24. W-J. Zhang, *J. Power Sources*, **196**, 2962 (2011).
25. M. Z. Bazant, *Faraday Discuss.*, **246**, 60 (2023).
26. M. He et al., *J. Power Sources*, **588**, 233741 (2023).
27. J. Huang et al., *Nat. Energy*, **5**, 674 (2020).